Available online at www.sciencedirect.com
SCIENCE DIRECT®
International Journal of Thermal Sciences 42 (2003) 397–406
International Journal of Thermal Sciences
www.elsevier.com/locate/ijts

Numerical investigation of natural convection inside a wavy enclosure

Prodip Kumar Das [1], Shohel Mahmud [*,2]

Department of Mechanical Engineering, Bangladesh University of Engineering and Technology, BUET, Dhaka-1000, Bangladesh

Received 26 February 2002; accepted 15 May 2002

Abstract

In this paper, hydrodynamic and thermal behaviors of fluid inside a wavy walled enclosure are investigated. The enclosure consists of two wavy and two straight walls. The top and the bottom walls are wavy and kept isothermal. Two vertical straight walls (right and left) are considered adiabatic. The integral forms of the governing equations are solved numerically using Finite Volume method. Computational domains are divided into finite numbers of body fitted control volumes with collocated variable arrangement. Results are presented in the form of local and global Nusselt number distributions for a selected range of Grashof number (10^3–10^7). Streamlines and isothermal lines are also presented for four different values (0.0, 0.05, 0.1, 0.15) of amplitude-wavelength ratios ($= \alpha/\lambda$) and for a fluid having Prandtl number 1.0. Throughout this study, aspect ratio ($= \delta/\lambda$) is kept equal to 0.40. Calculated results for Nusselt number are compared with the available references.

Keywords: Amplitude-wavelength ratio; Bi-cellular; Heat transfer; Multi-cellular; Natural convection; Wavy enclosure

1. Introduction

Natural convection heat transfer inside a wavy enclosure is one of the several devices employed for enhancing the heat and mass transfer efficiency. Heat transfer inside annular space, air-filled cavity or annular sector has wide application in many engineering problems like electronic packages, micro-electronic devices etc. The change of flow field with changes in surface waviness is a special feature of the complex corrugated-duct geometry that is not encountered in conventional ducts such as circular and annular pipes and rectangular ducts. In addition to the electronic packages and heat exchanger design, wavy geometry has also some geophysical applications like flows in the earth's crust. Geometrical complexity of such cavity or duct affects largely the flow pattern. Their fabrication depends on many parameters like amplitude, wavelength, phase angle, inter-wall spacing etc. Each of the parameter significantly affects the hydrodynamic and thermal behavior of fluid inside it. These configurations are not idealities and its effect on flow phenomenon motivates many researchers to perform experimental or analytical work on this topic.

Saidi et al. [1] presented numerical and experimental results of flow over and heat transfer from a sinusoidal cavity. They reported that the total heat exchange between the wavy wall of the cavity and the flowing fluid was reduced by the presence of vortex. Vortex plays the role of a thermal screen, which creates a large region of uniform temperature in the bottom of the cavity. Wang and Vanka [2] presented heat transfer and flow characteristics inside a wavy walled channel. Nishimura et al. [3] investigated flow characteristics such as flow pattern, pressure drop, and wall shear stress in a channel with symmetric sinusoidal wavy wall. Kumar [4] presented parametric results of flow and thermal field inside a vertical wavy enclosure embedded in a pours media. He concluded that the surface temperature was very sensitive to the drifts in the surface undulations, phase of the wavy surface, and number of the wave. Asako and Faghri [5] gave a Finite Volume prediction of heat transfer and fluid flow characteristics inside a wavy walled duct and tube, respectively. Lage and Bejan [6] documented heat

* Corresponding author.
E-mail addresses: pdas@ualberta.ca (P.K. Das), smahmud@engmail.uwaterloo.ca (S. Mahmud).
[1] Present address: Department of Mechanical Engineering, University of Alberta, Edmonton, AB T6G 2G8, Canada.
[2] Present address: Department of Mechanical Engineering, University of Waterloo, Waterloo, Ontario N2L3G1, Canada.

1290-0729/02/$ – see front matter
doi:10.1016/S1290-0729(02)00040-6

Nomenclature

a	dimensionless parameter $= \alpha/\lambda$		
$\boldsymbol{g}$	gravity vector	m·s^{-2}	
Gr	Grashof number $= \rho^2 g\beta\Delta T\delta^3/\mu^2$		
h	heat transfer coefficient	W·m^{-2}·K^{-1}	
k	thermal conductivity	W·m^{-1}·K^{-1}	
$\dot{m}$	mass flux	kg·s^{-1}	
Nu	Nusselt number (see Eqs. (17) and (18))		
$\hat{\boldsymbol{n}}$	unit normal vector		
Pr	Prandtl number $= \mu C_P/k$		
p	pressure	N·m^{-2}	
S	surface area	m^2	
T	temperature	K	
u_i	velocity component at i direction	m·s^{-1}	
u_j	velocity component at j direction	m·s^{-1}	
V	volume	m^3	
x	horizontal coordinate	m	
X	normalized axial distance $= x/\lambda$		
y	vertical coordinate	m	

Greek symbols

α	amplitude of the top and the bottom walls	m	
β	thermal expansion coefficient	K^{-1}	
δ	inter wall spacing between the top and the bottom walls	m	
λ	horizontal length of the cavity	m	
μ	dynamic viscosity	kg·m^{-1}·s^{-1}	
ϕ	any variable		
ρ	mass density	kg·m^{-3}	
Γ	diffusion coefficient		

Subscripts

av	average value
∞	at ambient condition
e	at the face 'e'
C	value based on cold wall
H	value based on hot wall
i, j	Cartesian notation of x and y direction
L	local value
w	value at wall
0	reference value

transfer results near a periodically (timewise and spatial) stretching wall. Adjlout et al. [7] reported natural convection in an inclined cavity with hot wavy wall and cold flat wall. One of their interesting findings was the decrease of average heat transfer with the surface waviness when compared with flat wall cavity.

In the present investigation, characteristics of natural convection inside a wavy enclosure are presented for an incompressible Newtonian fluid. Rate of heat transfer in terms of local and global Nusselt numbers are presented for different amplitude-wavelength ratios and Grashof numbers, respectively. Flow and thermal fields are analyzed by parametric presentations of streamlines and isothermal lines.

2. Mathematical modeling

In the present investigation, we take the advantage of Finite Volume method to generate body fitted grid with collocated variable arrangement. The integral forms of governing equations (continuity, momentum and energy) are as follows:

$$\int_S \rho \boldsymbol{v}\cdot\hat{\boldsymbol{n}}\,\mathrm{d}S = 0 \tag{1}$$

$$\int_S \rho u_i \boldsymbol{v}\cdot\hat{\boldsymbol{n}}\,\mathrm{d}S = \int_S \mu\,\mathrm{grad}\,u_i\cdot\hat{\boldsymbol{n}}\,\mathrm{d}S - \int_S p\mathbf{i}_i\cdot\hat{\boldsymbol{n}}\,\mathrm{d}S + \int_V \rho b_i\,\mathrm{d}V \tag{2}$$

$$\int_S \rho u_j \boldsymbol{v}\cdot\hat{\boldsymbol{n}}\,\mathrm{d}S = \int_S \mu\,\mathrm{grad}\,u_j\cdot\hat{\boldsymbol{n}}\,\mathrm{d}S - \int_S p\mathbf{i}_j\cdot\hat{\boldsymbol{n}}\,\mathrm{d}S + \int_V \rho b_j\,\mathrm{d}V \tag{3}$$

$$\int_S \rho T\boldsymbol{v}\cdot\hat{\boldsymbol{n}}\,\mathrm{d}S = \int_S k\,\mathrm{grad}\,T\cdot\hat{\boldsymbol{n}}\,\mathrm{d}S \tag{4}$$

where b_i and b_j is the body forces in the i and jth Cartesian directions. In cases considered here, the only body force is the buoyancy force, which is implemented by applying the Boussinesq approximation

$$\rho b_i = \rho_0 g_i \beta\,(T - T_0) \tag{5}$$

where g_i is the ith component of the gravity acceleration vector, T_0 is the reference temperature, and ρ_0 is the density at T_0. For present investigation, we used the following boundary conditions:

$$\begin{aligned}
&\text{Bottom wall: } 0 \leqslant x \leqslant \lambda \text{ and } y = \alpha - \alpha\cos(2\pi x);\\
&\qquad u_i = u_j = 0 \text{ and } T = T_H\\
&\text{Top wall: } 0 \leqslant x \leqslant \lambda \text{ and } y = \delta + \alpha - \alpha\cos(2\pi x);\\
&\qquad u_i = u_j = 0 \text{ and } T = T_C\\
&\text{Left wall: } x = 0 \text{ and } 0 \leqslant y \leqslant \delta;\\
&\qquad u_i = u_j = 0 \text{ and } \partial T/\partial n = 0\\
&\text{Right wall: } x = \lambda \text{ and } 0 \leqslant y \leqslant \delta;\\
&\qquad u_i = u_j = 0 \text{ and } \partial T/\partial n = 0
\end{aligned} \tag{6}$$

Eqs. (1)–(4) can be written in a generalized form

$$\int_S \rho\phi\boldsymbol{v}\cdot\hat{\boldsymbol{n}}\,\mathrm{d}S = \int_S \Gamma\,\mathrm{grad}\,\phi\cdot\hat{\boldsymbol{n}}\,\mathrm{d}S + \int_V q_\phi\,\mathrm{d}V \tag{7}$$

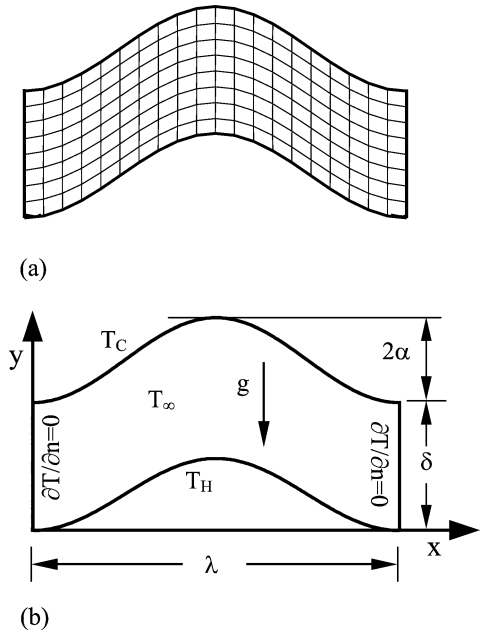

Fig. 1. Numerical grid structure and (b) computational domain.

Eqs. (1)–(4) are discretized using control-volume based Finite Volume method with collocated variable arrangement. Solution procedures with detail algorithm are available in references by Ferziger and Peric [8] and Patankar [9].

In Figs. 1(a) and 1(b), numerical grid structure and schematic diagram of the computational domain with geometrical parameters and boundary conditions used in present investigation are shown.

3. Numerical scheme

The Finite Volume method starts from the conservation equation in integral form

$$\int_S \rho\phi \boldsymbol{v}\cdot\hat{\boldsymbol{n}}\,\mathrm{d}S = \int_S \Gamma\,\mathrm{grad}\,\phi\cdot\hat{\boldsymbol{n}}\,\mathrm{d}S + \int_V q_\phi\,\mathrm{d}V \tag{8}$$

The solution domain is first subdivided into a finite number of contiguous control volumes (CVs), and the conservation equations are applied to each CV. At the centroid of each CV lies a computational node at which the variable values are to be calculated. The computational node at which all unknowns are stored in one-dimensional arrays and sorted level-wise, starting with level 1 (coarse grid) to level 3 (fine grid). Collocated arrangement is used for the variables, i.e., all variables are calculated at the same CV center. Both surface and volume integrals in the conservation equations (1)–(4) are approximated here using midpoint rule, i.e., the value of the integrand at the center of cell face or CV is multiplied by the face area or CV volume.

We look first at the calculation of mass fluxes. Only the East side of a 2D CV shown in Fig. 2 will be considered;

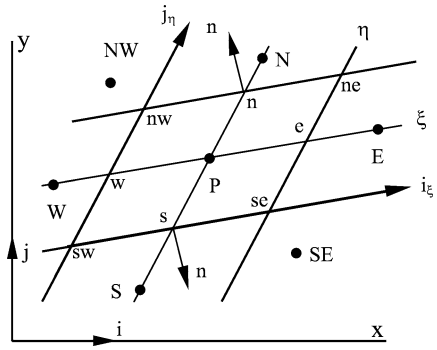

Fig. 2. A typical 2D-control volume and the notation used.

the same approach applies to other faces—only the indices need to be changed. The CV may have any number of faces; the analysis is not restricted to quadrilateral CVs like the one shown in Fig. 2. The midpoint rule approximation of the mass flux leads to:

$$\dot{m}_e = \int_{S_e} \rho\boldsymbol{v}\cdot\hat{\boldsymbol{n}}\,\mathrm{d}S \approx (\rho\boldsymbol{v}\cdot\hat{\boldsymbol{n}})_e S_e \tag{9}$$

The unit normal vector at the face 'e' is defined by

$$n_e S_e = S_e^i i_i = (y_{ne} - y_{se})i - (x_{ne} - x_{se})j \tag{10}$$

and the surface area, S_e is

$$S_e = \sqrt{\left(S_e^x\right)^2 + \left(S_e^y\right)^2} \tag{11}$$

With these definitions the expression for the mass flux becomes:

$$\dot{m}_e = \rho_e\left(S^x u_x + S^y u_y\right)_e \tag{12}$$

The difference between a Cartesian and a non-orthogonal grid is that, in the latter case, the surface vector has components in more than one Cartesian direction and all the velocity components contribute to the mass flux. Each Cartesian velocity component is multiplied by the corresponding surface vector component.

The convection flux of any transported quantity is usually calculated by assuming that the mass flux is known which, with the midpoint rule approximation, leads to

$$F_e^c = \int_{S_e} \rho\phi\boldsymbol{v}\cdot\hat{\boldsymbol{n}}\,\mathrm{d}S \approx \dot{m}_e\phi_e \tag{13}$$

where ϕ_e is the value of ϕ at the center of the cell face. The midpoint rule applied to the integrated flux gives

$$F_e^c = \int_S \Gamma\,\mathrm{grad}\,\phi\cdot\hat{\boldsymbol{n}}\,\mathrm{d}S \approx (\Gamma\,\mathrm{grad}\,\phi\cdot\hat{\boldsymbol{n}})_e S_e \tag{14}$$

The gradient of ϕ at the cell face center can be expressed either in terms of the derivatives with respect to global Cartesian coordinates of local orthogonal coordinates ($\boldsymbol{n}$, $\boldsymbol{t}$), e.g., in 2D:

$$\mathrm{grad}\,\phi = \frac{\partial\phi}{\partial x}\boldsymbol{i} + \frac{\partial\phi}{\partial y}\boldsymbol{j} = \frac{\partial\phi}{\partial n}\boldsymbol{n} + \frac{\partial\phi}{\partial t}\boldsymbol{t} \tag{15}$$

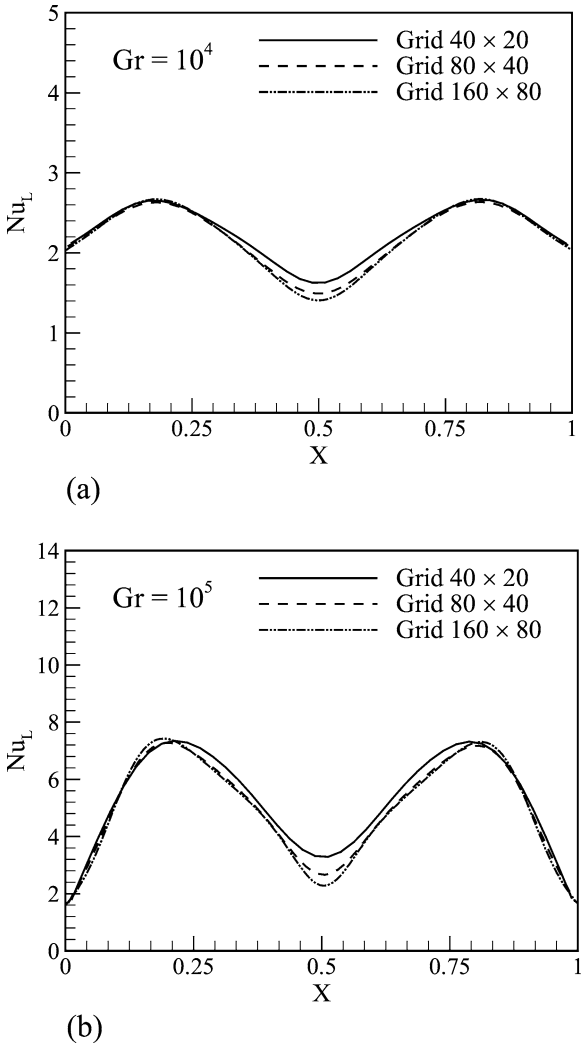

Fig. 3. Grid sensitivity test for (a) $Gr = 10^4$ and (b) $Gr = 10^5$, $a = 0.10$.

where ***n*** and ***t*** represent the coordinate direction normal and tangential to the surface, respectively.

If the variation of ϕ in the vicinity of the cell face is described by a shape function, it is then possible to differentiate this function at the 'e' location to find the derivatives with respect to the Cartesian coordinates. The diffusive flux is then

$$F_e^d = \Gamma_e \sum_i \left(\frac{\partial \phi}{\partial x_i}\right)_e S_e^i \tag{16}$$

This approximation is independent of the CV shape and is approximately of second order accurate. The final discretized form of governing equations is solved iteratively using Stone's SIP solver [8]. Iteration is continued until difference between two consecutive field values of variables is less than or equal to 10^{-4}. For further stabilization of numerical algorithm, under relaxation factors of 0.1–0.7 are used.

4. Results and discussions

Computations were carried out for three selected grid sizes (i.e., 40 × 20, 80 × 40, 160 × 80). Figs. 3(a) and 3(b) show Nusselt number distribution along the hot wall for Grashof numbers equal to 10^4 and 10^5, and amplitude-wavelength ratio, $a = 0.10$. Coarse grid (40 × 20) solution near the middle point of the hot wall of the cavity shows some deviation with the medium coarse and fine grids' solutions. Except this deviation, results for the selected grid sizes show good agreement with each other. Medium coarse (80 × 40) and fine (160 × 80) grids show almost same result. For better accuracy, fine grid (160 × 80) results are presented throughout this paper. For a particular amplitude-wavelength ratio (a), Grashof number was varied by changing the dynamic viscosity keeping other fluid and geometric variables constant.

For code validation, our numerical results are compared with the experimental results of Ozisic [10] and Bejan [11] for $a = 0.0$. Comparisons are presented in Fig. 4, where average Nusselt number is plotted as a function of Grashof number. Present prediction shows a very good agreement with the result of Ozisic [10] and a fair agreement with Bejan [11].

4.1. Heat transfer

Heat transfer rate is measured by local (Nu_L) and average (Nu_{av}) Nusselt numbers. Following equations are used to calculate the local and average Nusselt numbers:

$$Nu_L = \frac{\delta}{\Delta T}\left(\frac{\partial T}{\partial n}\right)_w \tag{17}$$

$$Nu_{av} = \frac{1}{\lambda}\int_0^{\lambda} Nu_L \,\mathrm{d}x \tag{18}$$

where the gradient term $(\partial T/\partial n)_w$ in Eq. (17) is the temperature gradient normal to the hot wall. Local Nusselt

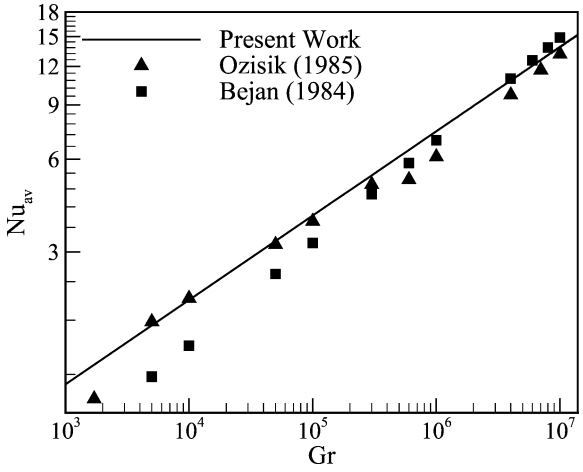

Fig. 4. Code validation of present work with other reference works.

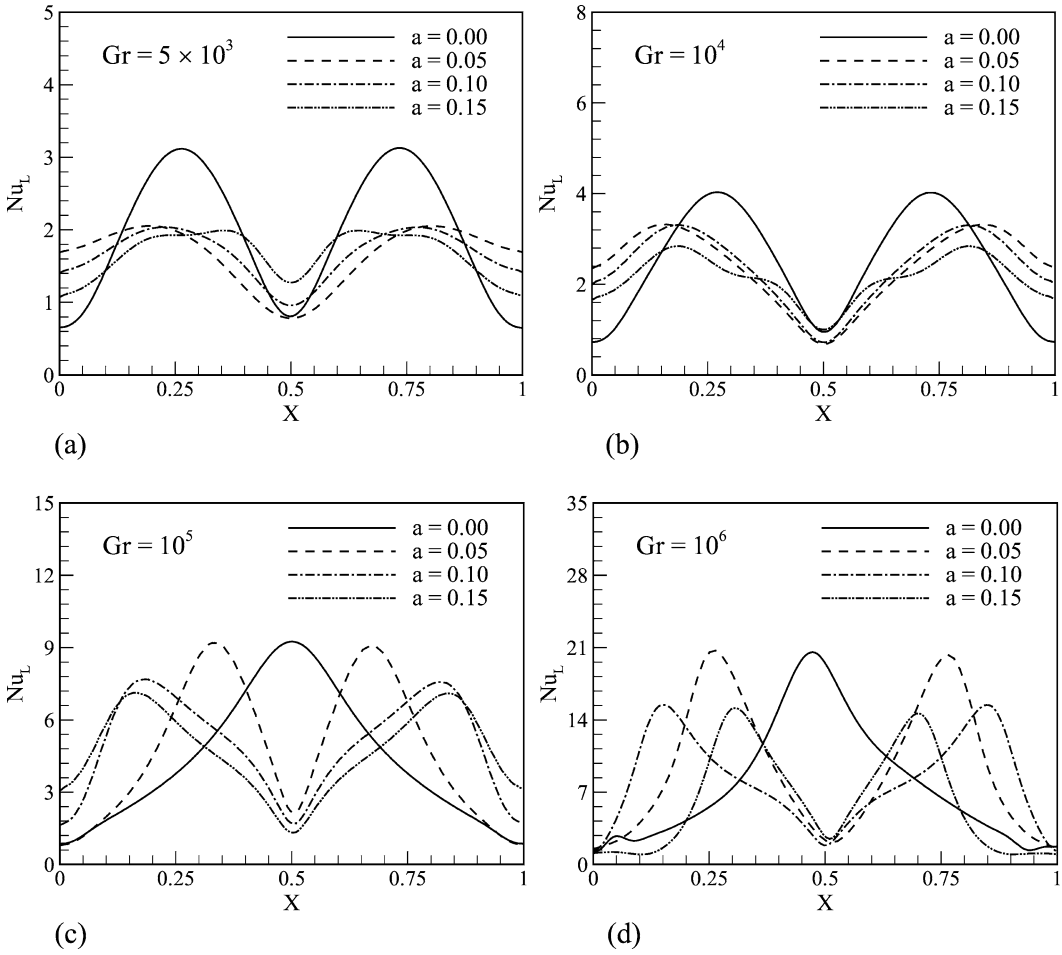

Fig. 5. Variation of local Nusselt number for different Grashof number.

number distribution is presented in Fig. 5 and Fig. 6. Average Nusselt number distribution is presented in Fig. 7. Detail discussions are presented in the following two sections.

4.2. Local heat transfer distribution

Local Nusselt number distribution at the bottom wall is shown in Figs. 5(a)–(d) for $Gr = 5 \times 10^3$, 10^4, 10^5, and 10^6. At $Gr = 5 \times 10^3$ and $a = 0.0$, Nusselt number distribution profile is symmetric with respect to $X = 0.5$ and shows a periodic nature of distribution with respect to the distance X. For $a = 0.05$, 0.10, and 0.15, Nu_L profiles are symmetric but no longer periodic as $a = 0.0$ case due to the surface waviness. For $a > 0$, two distinct zones are observed depending on the magnitude of the local Nusselt number. For $0.25 \leqslant X \leqslant 0.75$, Nu_L is higher in magnitude for higher a. Opposite scenario is observed for $X < 0.25$ and $X > 0.75$. This type of behavior of the Nu_L–X profile strongly depends on the Grashof number as shown in Figs. 5(b)–(d). At $Gr = 10^5$, Nu_L decreases with the increase of a at $X = 0.5$. Combined effects of multi-cellular flow and periodic swirling of isotherms (as we will see later) change the Nu_L–X profile to a periodic shape for $a > 0.0$, which differs from $a = 0$ case.

Local Nusselt number is plotted for constant amplitude-wavelength ratio (a) for different Grashof numbers ($= 10^3, 10^4, 10^5, 10^6$) in Figs. 6(a)–(d). At lower Grashof number, magnitude of Nusselt number is almost same along X direction for a particular a. Larger variation in the magnitude of Nu_L is observed at high Grashof numbers. For zero surface waviness ($a = 0$), peak value of Nu_L occurs at the line of symmetry ($X = 0.5$) for higher Grashof number. For $a > 0$, peak value of Nu_L occurs other than the line of symmetry as $a = 0$ case.

4.3. Average heat transfer distribution

The effect of amplitude-wavelength ratio on average heat rate transfer is shown in Fig. 7. At lower Grashof number the effect of amplitude-wavelength ratio is significant. However, at higher Grashof number this effect is very small. At higher amplitude-wavelength ratio heat transfer rate is higher at lower Grashof number when amplitude-wavelength ratio increase from zero to other values and after then, further increases of amplitude-wavelength ratio shows a negligible effect on average heat transfer rate.

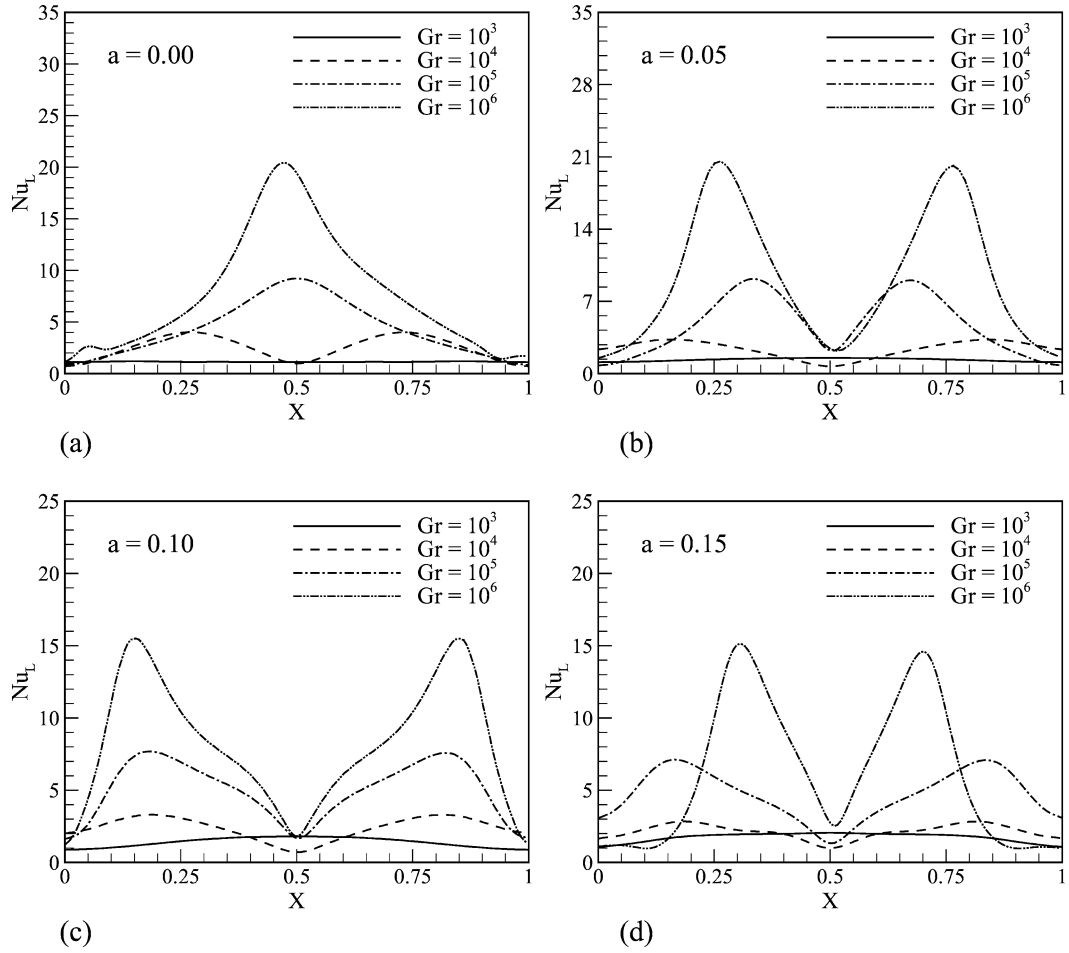

Fig. 6. Variation of local Nusselt number for different amplitude-wavelength ratio.

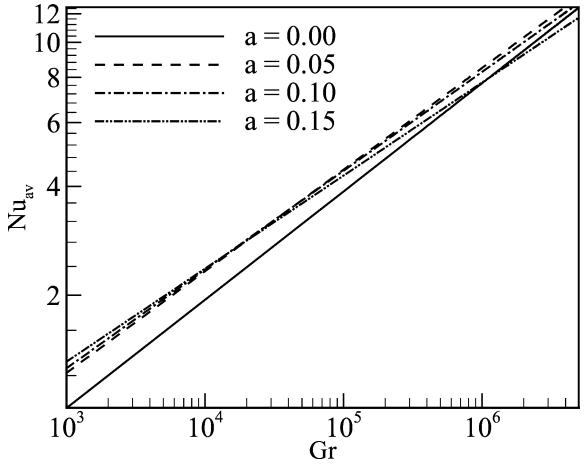

Fig. 7. Variation of average Nusselt number with Grashof numbers for different amplitude-wavelength ratio.

4.4. Flow field

Figs. 8(a)–(f) show the constant stream-function contours for six selected Grashof numbers for $a = 0.10$. At $Gr = 5 \times 10^3$, convection current inside the cavity is comparatively weak. Two counter rotating vortices with small cores are observed (Fig. 8(a)). This bi-cellular flow pattern divides the cavity into two symmetric parts with respect to the centerline ($X = 0.5$) of the cavity. Vortex at the left side and at the right side of the line of symmetry rotates counterclockwise and clockwise direction, respectively. At each half of the cavity, fluid stream near the hot wall tends to move towards the centerline of the cavity where two streams from the opposite direction mix and rise upwards. Vertical stream of the fluid splits into two streams (directed to the adiabatic walls) at the top wall of the cavity. This makes two counter rotating vortices (bi-cellular flow) inside the cavity. $Gr = 10^4$ is also characterized by the bi-cellular flow pattern but elongated core. At $Gr = 5 \times 10^4$, multi-cellular flow appears with four vortices. Due to comparatively high buoyant effect, another vertical stream of the fluid appears near the adiabatic walls. Considering one half of the cavity, one stream of fluid (at the top wall) moves towards the adiabatic wall from the symmetry line and another stream moves towards the symmetry line from the adiabatic wall. These two opposite streams produce a downward stream of the fluid at their intersection, thus producing two counter rotating vortices at each half of the cavity. Further increase of Grashof number ($Gr = 10^5$ and 2×10^5) increases the strength of the vortices, keeping four-cell multi-cellular flow pattern

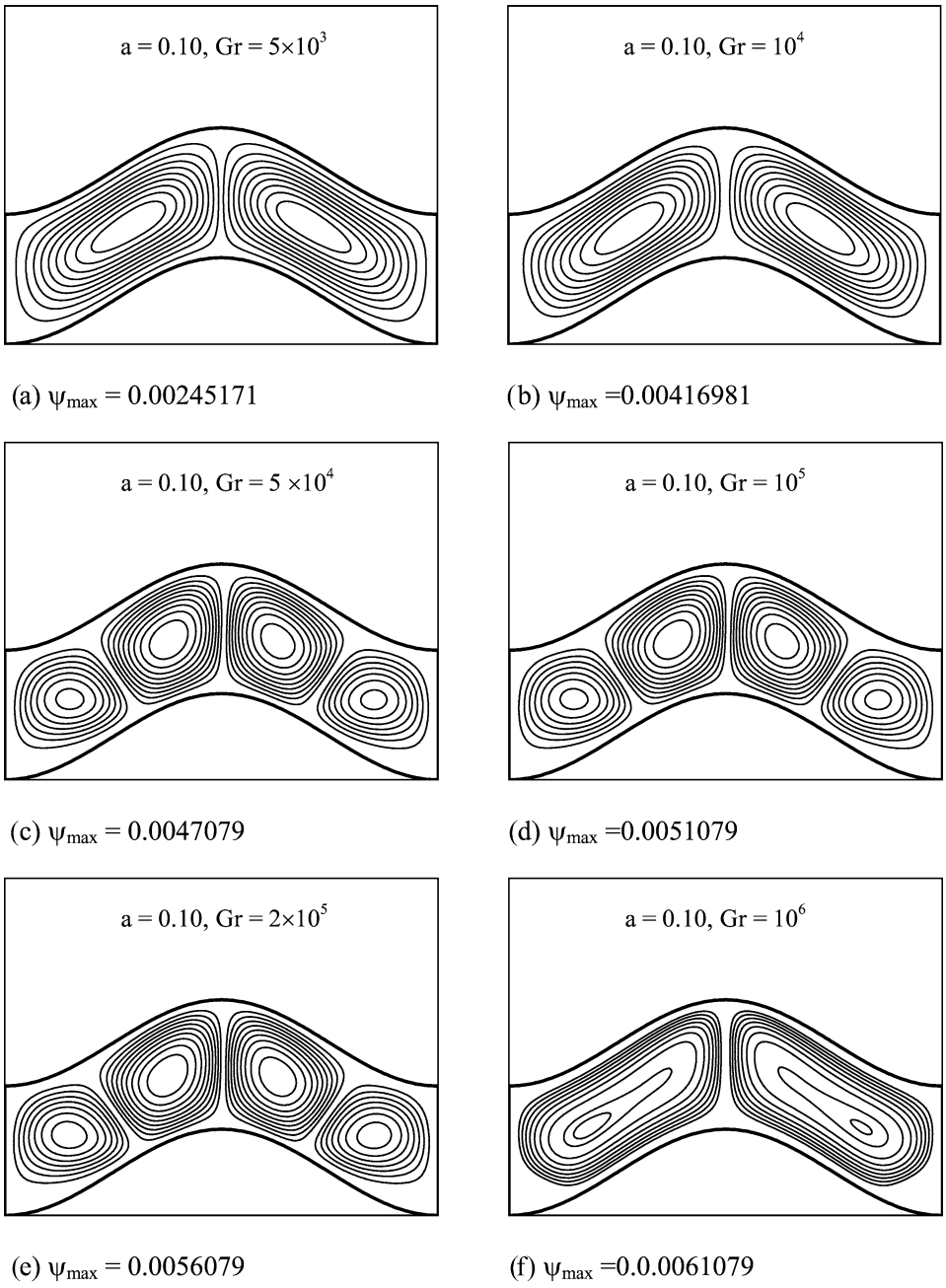

Fig. 8. Streamlines for different Grashof number for $a = 0.10$.

inside the cavity. The overall physics of flow will be more clear to understand when thermal field will be presented and discussed later. An interesting reverse transition occurs at $Gr = 10^6$. Multi-cellular flow patterns turns into a bi-cellular flow at this Grashof number ($= 10^6$). This bi-cellular flow pattern is qualitatively different from the flow pattern at $Gr \leqslant 10^4$. High convection current shifts the core of each vortex towards the adiabatic wall of the cavity.

Fig. 9 shows the effect of amplitude-wavelength ratio (a) on flow field at constant Grashof number ($= 5 \times 10^4$). Whatever the value of a, flow inside the cavity is characterized by a four-cell multi-cellular pattern. An increase in the value of a increases the size of two vortices near the line of symmetry and decreases the size near the adiabatic walls.

4.5. Velocity vector

To facilitate our understanding of flow field, velocity vector is plotted in Figs. 10(a)–(c) for $a = 0.10$ and $Gr = 10^4$, 5×10^4, and 5×10^5. For all Grashof numbers, a vertical stream of fluid (velocity vectors are directed upward) at the line of symmetry characterizes the flow. At $Gr = 10^4$, velocity profiles are similar to the profile inside a shallow cavity [11] except at or near the line of symmetry and close

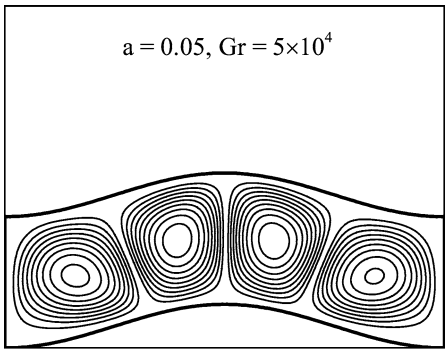

(a) ψ_{max} =0.00497852

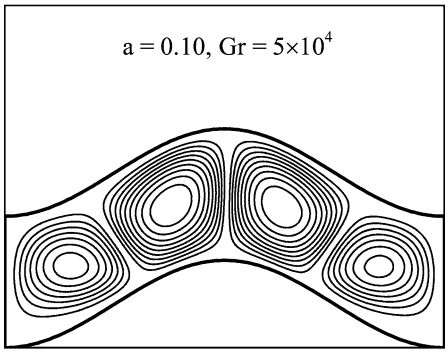

(b) ψ_{max} =0.0047079

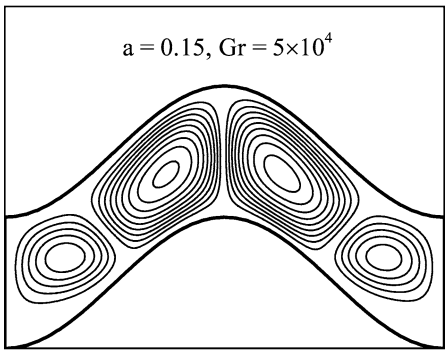

(c) ψ_{max} =0.00436513

Fig. 9. Streamlines for different amplitude-wavelength ratio for $Gr = 5 \times 10^4$.

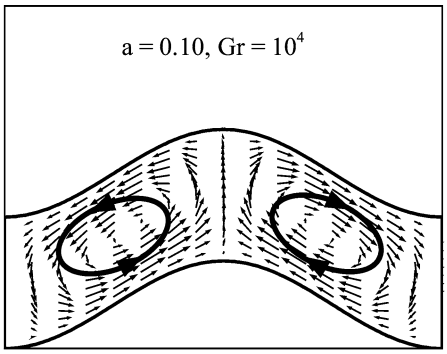

(a)

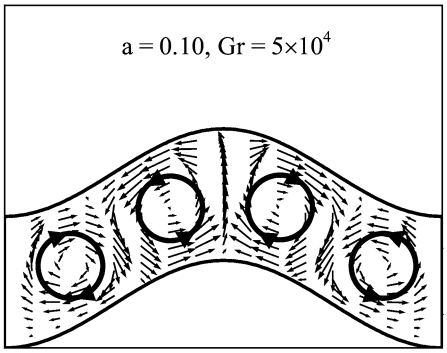

(b)

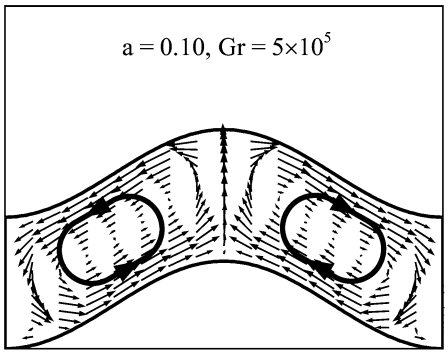

(c)

Fig. 10. Velocity Vector for different Grashof numbers for $a = 0.10$.

to the adiabatic walls. Two small ellipsis with arrow marks show the motion and rotational direction of the fluid inside the cavity at this Grashof number. Except at the walls, a thin layer of fluid is almost motionless (stagnant) approximately at the center of each ellipse. Direction of the fluid motion above and below this stagnant fluid is opposite. At $Gr = 5 \times 10^5$, flow is multi-cellular as already described in previous section which is supported by the direction of velocity vectors. Four small circles with arrow marks facilitate to understand the direction of motion of the fluid. Fluid is motionless at the center of each circle. Flow at $Gr = 5 \times 10^5$ is bi-cellular but qualitatively different from the bi-cellular flow pattern at $Gr = 10^4$. Boundary layer forms due to the high convection current and a large portion of the fluid is stagnant at the center of the each half of the cavity (see Fig. 10(c)).

4.6. Thermal field

Thermal fields are presented in the form of isothermal lines in Figs. 11(a)–(f) for $a = 0.10$ and for some selected values of Grashof numbers as indicated in figures. For the convenience of analysis, temperature is made dimensionless using the expression $(T - T_\infty)/(T_H - T_C)$ so that the values of temperatures fall in between 0 and 1 in each figure. Twenty contours are plotted in each figure with the interval 0.05. At $Gr = 5 \times 10^3$, buoyancy effect is negligible.

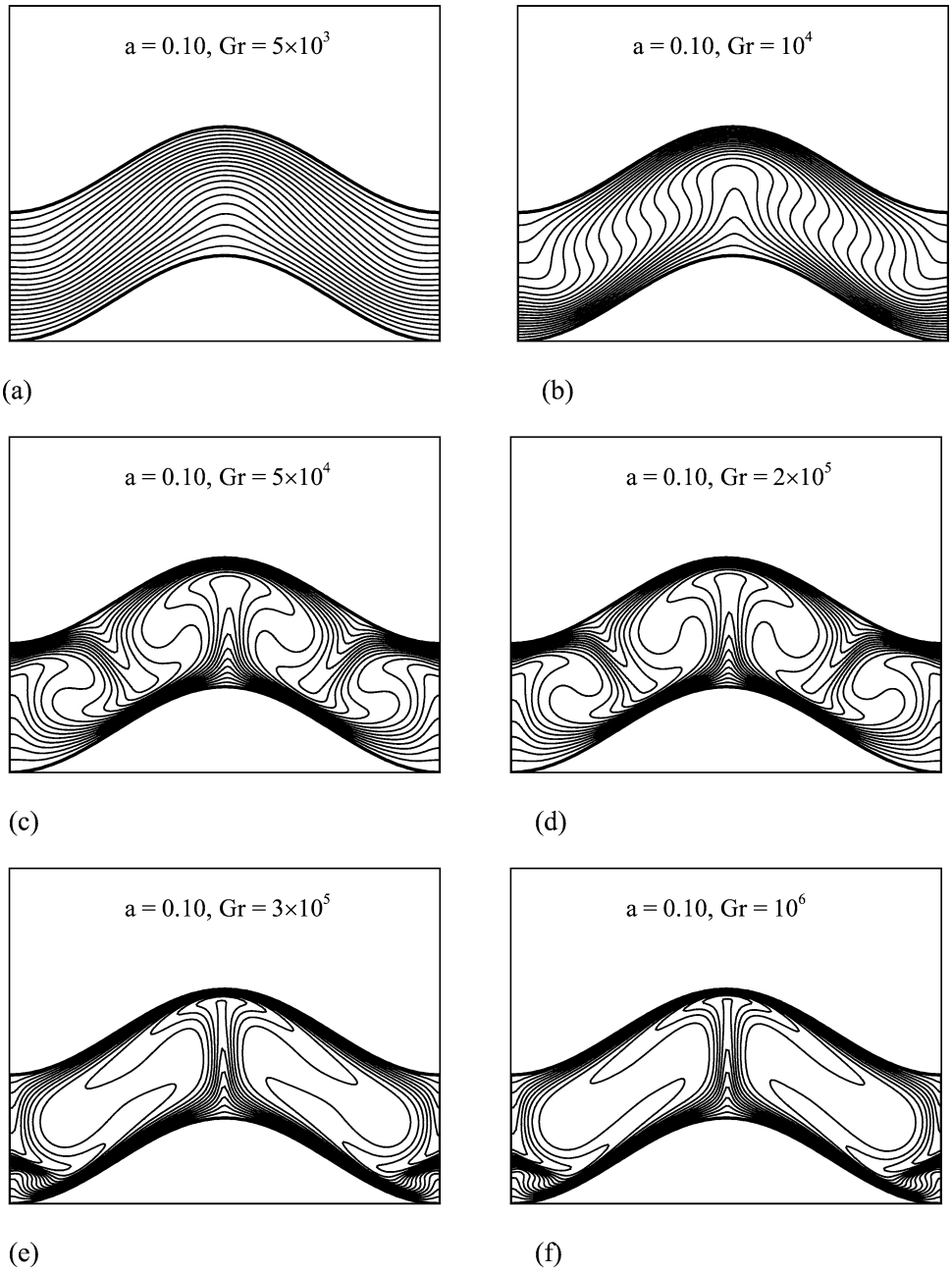

Fig. 11. Isothermal lines for different Grashof numbers for $a = 0.10$.

Isothermal lines are nearly parallel to each other and follow the geometry of the wavy surfaces. Some deviation is observed near the hot wall around the centerline ($X = 0.5$) of the cavity due the effect of upward fluid stream. Isothermal lines swirl at $Gr = 10^4$ due the influence of convection current. Two hot spots appear near the bottom wall, where isothermal lines are concentrated, leaving high temperature gradient. Heat transfer rate is higher in magnitude at the hot spots. A periodic swirling of isothermal lines appear at $Gr = 5 \times 10^4$ and 2×10^5 due the appearance of multi-cellular flow (see Figs. 8(c)–(e)). Hot spots elongate along the bottom wall with the increase of Grashof number. At $Gr = 3 \times 10^5$ and 10^6, periodic swirling nature of isothermal lines disappears due to the occurrence of reverse transition in flow field. Hot spots almost occupy the bottom wall of the cavity. Heat transfer rate is very high as already indicated in Fig. 5.

5. Conclusion

Buoyancy induced flow and heat transfer inside a wavy enclosure with two wavy walls and two straight walls are investigated numerically. Amplitude-wavelength ratio affects both local heat transfer rate and flow field as well as thermal field. Increasing amplitude-wavelength ratio changes the true periodic nature of the local Nusselt number distribu-

tion at higher Grashof number and has a little effect at lower Grashof number. Amplitude-wavelength ratio has no significant influence on average heat transfer rate. Only at lower Grashof number, heat transfer rate rises when amplitude-wavelength ratio changes from zero to other values, after then it has almost negligible effect on average heat transfer rate. At lower Grashof number, flow field is characterized by the appearance of bi-cellular pattern, which turns into multi-cellular pattern at higher Grashof numbers. Further increase of Grashof number causes the reverse transition by changing the multi-cellular flow into bi-cellular.

References

[1] C. Saidi, F. Legay, B. Pruent, Laminar flow past a sinusoidal cavity, Internat. J. Heat Mass Transfer 30 (1987) 649–660.
[2] G. Wang, S.P. Vanka, Convective heat transfer in periodic wavy passages, Internat. J. Heat Mass Transfer 38 (1995) 3219–3230.
[3] T. Nishimura, Y. Ohori, Y. Kawamura, Flow characteristics in a channel with symmetric wavy wall for steady flow, J. Chemical Engrg. Japan 17 (1984) 466–471.
[4] B.V.R. Kumar, A study of free convection induced by a vertical wavy surface with heat flux in a porous enclosure, Numer. Heat Transfer A 37 (2000) 493–510.
[5] Y. Asako, M. Faghri, Finite volume solution for laminar flow and heat transfer in a corrugated duct, J. Heat Transfer 109 (1987) 627–634.
[6] J.L. Lage, A. Bejan, Convection from a periodically stretching plane wall, J. Heat Transfer 112 (1990) 92–99.
[7] L. Adjlout, O. Imine, A. Azzi, M. Belkadi, Laminar natural convection in an inclined cavity with a wavy wall, Internat. J. Heat Mass Transfer 45 (2002) 2141–2152.
[8] J. Ferziger, M. Peric, Computational Methods for Fluid Dynamics, Springer-Verlag, Berlin, 1996.
[9] S.V. Patankar, Numerical Heat and Mass Transfer and Fluid Flow, McGraw-Hill, New York, 1980.
[10] M.N. Ozisik, Heat Transfer a Basic Approach, McGraw-Hill, New York, 1985.
[11] A. Bejan, Convective Heat Transfer, John Wiley, New York, 1984.